

# An Experimental Multi-Band Channel Characterization in the Upper Mid-Band

Roberto Bomfin\*, Ahmad Bazzi\*<sup>◇</sup>, Hao Guo<sup>◇§</sup>, Hyeongtaek Lee<sup>†</sup>,  
Marco Mezzavilla<sup>‡</sup>, Sundeep Rangan<sup>◇</sup>, Junil Choi<sup>†</sup>, and Marwa Chafii\*<sup>◇</sup>

\*Engineering Division, New York University Abu Dhabi, UAE

<sup>◇</sup>NYU WIRELESS, NYU Tandon School of Engineering, New York, USA

<sup>§</sup>Department of Electrical Engineering, Chalmers University of Technology, Gothenburg, Sweden

<sup>†</sup>School of Electrical Engineering, KAIST, Republic of Korea

<sup>‡</sup>Dipartimento di Elettronica, Informazione e Bioingegneria (DEIB), Politecnico di Milano, Milan, Italy

Email: roberto.bomfin@nyu.edu, ahmad.bazzi@nyu.edu, hg2891@nyu.edu, htlee8459@kaist.ac.kr,

marco.mezzavilla@polimi.it, srangan@nyu.edu, junil@kaist.ac.kr, marwa.chafii@nyu.edu

**Abstract**—The following paper provides a multi-band channel measurement analysis on the frequency range (FR)3. This study focuses on the FR3 low frequencies 6.5 GHz and 8.75 GHz with a setup tailored to the context of integrated sensing and communication (ISAC), where the data are collected with and without the presence of a target. A method based on multiple signal classification (MUSIC) is used to refine the delays of the channel impulse response estimates. The results reveal that the channel at the lower frequency 6.5 GHz has additional distinguishable multipath components in the presence of the target, while the one associated with the higher frequency 8.75 GHz has more blockage. The set of results reported in this paper serves as a benchmark for future multi-band studies in the FR3 spectrum.

**Index Terms**—Channel Modeling, Frequency Range (FR)3, Multi-Band, Integrated Sensing and Communication (ISAC).

## I. INTRODUCTION

The demand for new frequency bands such as Frequency Range (FR)3 arises from the congestion in the sub-6 GHz spectrum and limitations of millimeter wave (mmWave) frequencies. Sub-6 GHz bands, though widely used in cellular systems up to 4G, face severe spectral shortages. While mmWave offers large bandwidths for multi-gigabit data rates in 5G, it suffers from limited transmission range and high blockage sensitivities, leading to inconsistent performance. FR3, covering 7 to 24 GHz, presents a compelling alternative, balancing coverage and capacity, and is increasingly seen as a key resource for 5G-Advanced and 6G networks [1], [2].

FR3 offers more spectrum than sub-6 GHz bands while retaining better propagation characteristics compared to mmWave frequencies. This makes it ideal for cellular services that require a balance of bandwidth and coverage. However, there are existing services partially occupying the FR3 bands, e.g., military radar, radio astronomy, and satellite communications, which makes spectral sharing crucial here [2]. Regulatory bodies, such as the FCC, have started identifying parts of the FR3 spectrum for cellular use, highlighting its growing importance in future spectrum allocations [3].

Channel measurements in FR3 are crucial for understanding its propagation characteristics and optimizing its use across

various applications [4], [5]. While recent measurement campaigns have gathered valuable data on, e.g., channel impulse response (CIR), there remains a significant gap in applying FR3 to target detection, particularly in challenging environments [6]. The ability to use FR3 frequencies for detecting objects, especially in scenarios where line-of-sight (LoS) is weak or partially blocked, holds great potential for applications such as autonomous vehicles and radar-based sensing systems. However, the behavior of FR3 frequencies in target detection is not yet fully understood, and existing models do not adequately capture the correlations across multiple frequencies that are necessary for accurate detection [7]. Developing more adaptive models based on detailed multi-frequency measurements is essential for fully realizing the potential of FR3 in these critical sensing applications.

In this paper, we conduct a multiple-antenna multi-band channel measurement campaign in the low FR3 region, in particular, at 6.5 GHz<sup>1</sup> and 8.75 GHz. In our system, we make use of the newly developed Pi-Radio radio frequency (RF) frontend [6], which is capable of up-converting signals spanning the whole FR3 range. Moreover, with the recent studies of integrated sensing and communication (ISAC) in the literature [8]–[11], we focus our investigation on comparing the multi-frequency channel measurements in the presence of a target. In this initial set of results reported in this paper, we investigate how the impulse response changes from frequency to frequency and provide insights for ISAC. In terms of processing techniques, we utilize a similar method to [12] where a multiple signal classification (MUSIC)-type algorithm is applied on discrete-time channel impulse response to provide a refined delay estimation of the multipath. The novelty of this work consists of performing the multi-band channel measurement at the new FR3 spectrum and developing a methodology for the data analysis. The results reveal that the channel at the lower frequency 6.5 GHz has additional multi-

<sup>1</sup>While this frequency is at the edge of FR3, we avoid making this distinction explicitly for simplicity.

path components in the presence of the target, while the higher frequency 8.75 GHz has more blockage. This demonstrates a difference in how the target can alter the background channel (or clutter) depending on the frequency. The methodology and results presented in this paper will serve as a benchmark for future measurements in the FR3 regions. The contributions of this paper are summarized as

- **Multi-band multi-antenna measurement in the new FR3 spectrum**, at 6.5 GHz and 8.75 GHz, utilizing the Pi-Radio RF frontend, which supports *the entire FR3 range*. Our compact platform allows us to conduct FR3 measurements over multi-frequency channel measurements in the presence/absence of a target.
- **Methodology for ISAC channel characterization**, so as to highlight the prominent multipath components and cluster them into delay groups that are close to each other. It operates on a frame-by-frame basis, utilizing frequency-domain subcarrier smoothing to de-correlate the multipath components. Subsequently, a  $K$ -means clustering algorithm is employed, using a silhouette-based criterion to determine the number of delay clusters.
- **Insights for ISAC and benchmark for future multi-band measurement campaigns**. Insights reveal distinct characteristics between different FR3 frequencies. For instance, the presence of the target can introduce new paths or block previously existing ones differently for each frequency. This effect is further analyzed using positive and negative regions, which highlight the correlation of the target with the environment it is placed in.

## II. SYSTEM MODEL

### A. Transmit Sequences

Our system is  $2 \times 1$  multiple-input single-output (MISO), where two orthogonal sequences are transmitted in each antenna. The discrete-frequency domain signal associated with the first antenna, subscript a, is  $\mathbf{X}_a \in \mathcal{S}_{\text{QPSK}}^{N_{\text{on}}}$ , where  $\mathcal{S}_{\text{QPSK}}$  is the set of quadrature phase-shift keying (QPSK) symbols, and  $N_{\text{on}}$  is the number of allocated subcarriers centered at the middle of the spectrum. We generate an orthogonal signal for the second antenna, subscript b, as  $\mathbf{X}_b[k] = \mathbf{X}_a[k]e^{j2\pi k/2} \forall k \in [-N/2 + 1, N/2]$  so that its discrete-time domain counterpart is  $\mathbf{x}_b = \mathbf{x}_a \circledast \boldsymbol{\delta}_{N/2}$ , where  $\boldsymbol{\delta}_i[n]$  is the Kronecker delta vector with 1 for  $i = n$  and 0 otherwise, and  $\circledast$  represents the circular convolution. The quantity  $N$  represents the fast Fourier transform (FFT) size. Assuming a limited delay spread smaller than  $N/2$  samples, the above property enables an easy MISO channel estimation by windowing the discrete-time domain channel estimate, as shown in [13]. The transmit signal at antenna a is

$$\tilde{x}_a(t) = \sum_{n=-\infty}^{\infty} \tilde{\mathbf{x}}_a[n]g_t(t - n/B), \quad (1)$$

where  $g_t(t)$  is the band-limited transmit filter with bandwidth  $B$ , and  $\tilde{\mathbf{x}}_a = [\mathbf{x}_a^T \mathbf{x}_a^T \cdots]$  is a concatenation of  $\mathbf{x}_a$  to describe its constant transmission. Lastly, the input for antenna b is obtained analogously.

### B. Wireless Channel Model

In this work, we explore transmissions in two different frequencies, namely,  $f_c = 6.5$  GHz and 8.75 GHz. The small-scale parameters such as the amplitude of each path,  $\alpha_{a,f_c,l}$ , are considered to be frequency-dependent due to the different reflection coefficients of objects. The delay per path,  $\tau_{l,a}$ , and the total number of delays,  $L_a$ , are considered to be the same for both frequencies since they depend on the environmental geometry. With the above considerations, the channel impulse response between the antenna a and the receiver is defined as

$$h_{a,f_c}(t) = \sum_{l=0}^{L_a-1} \alpha_{a,f_c,l} \delta(t - \tau_{l,a}), \quad (2)$$

which is assumed to be time-invariant. The received signal for  $2 \times 1$  MIMO system is given by the convolution between the transmitted signal and channel

$$\tilde{y}_{f_c}(t) = \sum_{l=0}^{L_a-1} \alpha_{a,f_c,l} \tilde{x}_a(t - \tau_{l,a}) + \sum_{l=0}^{L_b-1} \alpha_{b,f_c,l} \tilde{x}_b(t - \tau_{l,b}) + w(t), \quad (3)$$

where  $w(t)$  is the additive white Gaussian noise (AWGN).

### C. Channel Estimation

Let  $y_{f_c}(t) = \tilde{y}_{f_c}(t) * g_r(t)$  be the filtered signal at the receiver, where  $\mathbf{y}_{f_c}[n] = y_{f_c}(n/B)$  for  $n \in [0, N - 1]$  is the sampled received signal and  $\mathbf{Y}_{f_c}$  its DFT. The discrete-frequency channel is obtained as  $\mathbf{R}_{a,f_c}[k] = \mathbf{Y}_{f_c}[k]/\mathbf{X}_a[k]$ , which contains the channels  $h_{a,f_c}$  and  $h_{b,f_c}$  due to (3). The discrete-time channel impulse response for the antennas a and b are obtained by filtering the discrete-time signal  $\mathbf{r}_{a,f_c} = \text{IDFT}(\mathbf{R}_{a,f_c})$  as [13]

$$\begin{aligned} \hat{\mathbf{h}}_{a,f_c}[n] &= \mathbf{r}_{a,f_c}[n], \quad 0 \leq n < N/4 \\ \hat{\mathbf{h}}_{b,f_c}[n] &= (\mathbf{r}_{a,f_c} \circledast \boldsymbol{\delta}_{-N/2})[n], \quad 0 \leq n < N/4, \end{aligned} \quad (4)$$

where  $\hat{\mathbf{h}}_{a,f_c}[n] = \hat{\mathbf{h}}_{b,f_c}[n] = 0$  for  $n \geq N/4$ . This operation assumes that the first delays  $\tau_{0,a} \approx \tau_{0,b} < 1/B$ , which can be forced by appropriately shifting  $\mathbf{r}_{a,f_c}$  without problem since we are not interested in the absolute delays. Lastly, the estimates of (4) in the frequency domain  $\hat{\mathbf{H}}_{a,f_c}, \hat{\mathbf{H}}_{b,f_c} \in \mathbb{C}^{N_{\text{on}}}$  are defined such that they contain only the allocated carriers.

## III. DATA PROCESSING METHODS

### A. 2<sup>nd</sup>-order Elbow Method & MUSIC-PDP

In general, the covariance matrix associated with the parameters to be estimated plays a crucial role in numerous algorithms especially in array signal processing [14]. Notice that we decompose the  $\mathbb{C}^{N_{\text{on}} \times N_{\text{on}}}$  covariance matrix of the channel estimates as

$$\mathbf{C}_{a,f_c} = \mathbb{E} \left[ \hat{\mathbf{H}}_{a,f_c} \hat{\mathbf{H}}_{a,f_c}^H \right] = \mathbf{B}_a \boldsymbol{\alpha}_{a,f_c} \boldsymbol{\alpha}_{a,f_c}^H \mathbf{B}_a^H + \mathbf{W}_{a,f_c}, \quad (5)$$

where  $\boldsymbol{\alpha}_{a,f_c} \in \mathbb{C}^{L_a}$  is obtained by stacking up all elements of  $\alpha_{a,f_c,l}$  in vectorized form. Moreover,  $\mathbf{B}_a$  is an  $N_{\text{on}} \times L_a$  matrix containing the path delays each parameterized within a column of  $\mathbf{B}_a$ . Finally,  $\mathbf{W}_{a,f_c}$  is the covariance matrix of the noise process at carrier  $f_c$  and antenna a. An analogous

expression for antenna b. It is straightforward to see that the signal subspace embedded within  $\mathbf{C}_{a,f_c}$  is rank-1, where the underlying reason being that multipath channels are known to give rise to coherent signals [15], i.e. each path is nothing but a *scaled and delayed* version of another. This, in turn, implies that eigenmode analysis techniques do not directly reflect the total number of multipath components contained within a wireless propagation channel.

To remedy the rank-deficiency, we apply some well-known smoothing techniques across frequency domain [16]. Specifically, a space-frequency smoothing technique decorrelates the multipath components, hence restoring the rank of the signal subspace for eigenmode analysis purposes. The outcome of the smoothing process is a smaller, but smoothed, covariance matrix version of (5), expressed as  $\tilde{\mathbf{C}}_{a,f_c} = \tilde{\mathbf{B}}_a \boldsymbol{\alpha}_{a,f_c} \boldsymbol{\alpha}_{a,f_c}^H \tilde{\mathbf{B}}_a^H + \tilde{\mathbf{W}}_{a,f_c} \in \mathbb{C}^{\tilde{N} \times \tilde{N}}$  where now  $\tilde{\mathbf{B}}_a$  is an  $\tilde{N} \times L_a$  with  $\tilde{N} < N_{\text{on}}$ . After smoothing, a principle component analysis study is done via eigenvalue decomposition (EVD), which is performed on  $\tilde{\mathbf{C}}_{a,f_c}$  for model order selection. For this purpose, the eigenvalues are sorted in a vector  $\lambda_{a,f_c}$ , whereby an elbow-type method identifies an optimal index in  $\lambda_{a,f_c}$  to determine the number of multipath components. The elbow method is based on the second-order statistics of the eigenvalues [17]. This optimal index, i.e. the *elbow* point, should appear at  $L_a$  eigenvalues, suggesting that the majority of the explained variability in the data can be captured within  $L_a$  dimensions, with minimal loss of information. After estimating  $L_a$ , denoted as  $\hat{L}_a$ , we can now apply state-of-the-art parameter estimation methods, where we have chosen MUSIC due to its ease of implementation. The frequency-based smoothed MUSIC-power delay profile (PDP) spectrum is formed as

$$P_{a,f_c}(\tau) = \|\mathbf{b}^H(\tau) \mathbf{U}_{a,f_c}^{\text{noise}}\|^{-2}, \quad (6)$$

where  $\mathbf{U}_{a,f_c}^{\text{noise}}$  corresponds to the noise subspace obtained from  $\mathbf{C}_{a,f_c}$ . It is worth noting that a MUSIC-PDP is much more robust to process compared to a classical PDP spectrum because filters out outliers and tests for paths in the spectrum under maximum orthogonality, as per its criterion in (6). After delay estimation, the path gains can be obtained by a simple inversion criterion.

### B. *K*–Means Clustering of multipath delays

The *K*–Means is a commonly known and widely used clustering mechanism that aims at partitioning a given dataset into *K* clusters. In our problem, it allows us to group the relative delays, relative to the first arriving path, clusters that are somehow close to one another. For each symbol, the peaks of the MUSIC-PDP are collected and stored, as explained in Section III-A. These delay estimates are passed to a *K*–means clustering algorithm, that groups these delay estimates into groups. The *K*–means clustering minimizes the sum of squared distances between the delay estimates and the clustered delay centroids, i.e. the objective would be to minimize the overall *within-cluster sum of squares* clustering cost as

$$\{\mathcal{T}_1^{\text{opt}} \dots \mathcal{T}_K^{\text{opt}}\} = \arg \min_{\mathcal{T}_1 \dots \mathcal{T}_K} \sum_{i=1}^K \sum_{\tau_j \in \mathcal{T}_i} \|\tau_j - c_i\|^2,$$

where for sake of simplicity we denote all the collected delay estimates as  $\tau_j$  and  $c_i$  represents the clustered delay centroid of the  $i^{\text{th}}$  cluster. Due to lack of space, we omit the details of the *K*–means clustering algorithm. Moreover, we adopt a silhouette-type method, which reports how distinguishable the delay clusters  $\mathcal{T}_1^{\text{opt}} \dots \mathcal{T}_K^{\text{opt}}$  are separated in order to determine the optimal number of delay clusters. In short, the optimal number of clusters is the one that maximizes the so-called average silhouette score, which is the average of all silhouette coefficients, which for a given delay estimate is computed as  $\xi(\tau_i) = \frac{\phi(\tau_i) - \Phi(\tau_i)}{\max\{\Phi(\tau_i), \phi(\tau_i)\}}$ , where  $\Phi(\tau)$  is the average distance from  $\tau$  to all other points in the same cluster, where  $\phi(\tau)$  is minimum average distance from  $\tau$  to all points in neighboring delay clusters.

## IV. EXPERIMENTAL SETUP

### A. Hardware

To implement our experiment in FR3, we propose and verify a novel software-defined radio (SDR) platform for FR3, which can be configured as a transmitter (TX) or receiver (RX). We design a system with 2 transmit and 2 receive chains. The basic components of the proposed upper mid-band SDR platform can be summarized as follows:

- **Digital baseband board - RFSoc ZCU111:** This evaluation Kit features the Zynq UltraScale+ XCZU28DR, integrating eight 12-bit analog-to-digital converters (ADCs) and eight 14-bit digital-to-analog converters (DACs) with maximum sample rates of 4.096 Gsps and 6.554 Gsps, respectively. In our system, we utilize a Matlab interface to transfer baseband samples to and from the RFSoc.
- **RF transceiver (TRX) board - Pi-Radio board:** The Pi-Radio TRX board performs the up and down-conversion to 2 transmit and 2 receive intermediate frequency (IF) streams. This two-stage up- and down-conversion is used to meet the out-of-band and adjacent channel rejection ratio requirements and strict spectral masks. More details of the board can be found at [6].
- **Antenna - Kyocera patch antenna:** The Kyocera 1005193 is a ultra wideband (UWB) printed circuit board (PCB) antenna designed for operation over the 6.0–8.5 GHz frequency range<sup>2</sup>. It offers a peak gain of 6.0 dBi, and has compact dimensions of 18.6 x 20.6 x 0.8 mm with easy integration with the Pi-Radio board.

### B. Environment

Our measurement campaign was performed in an indoor laboratory of NYU WIRELESS as shown in Fig. 1 on the next page. To have diversity in the data, we set the various locations of the TX and RX. In addition, the measurements were conducted with and without the presence of a metallic structure denoted as the target. The locations of the TX, RX, and target are depicted in Fig. 2a. With the fixed locations for the TX and target, we considered five different RX locations,

<sup>2</sup>We have experimentally verified that these antennas can be used at 8.75 GHz.



Fig. 1: Measurement environment at NYU Wireless, Brooklyn, NY, USA (<https://wireless.engineering.nyu.edu/>).

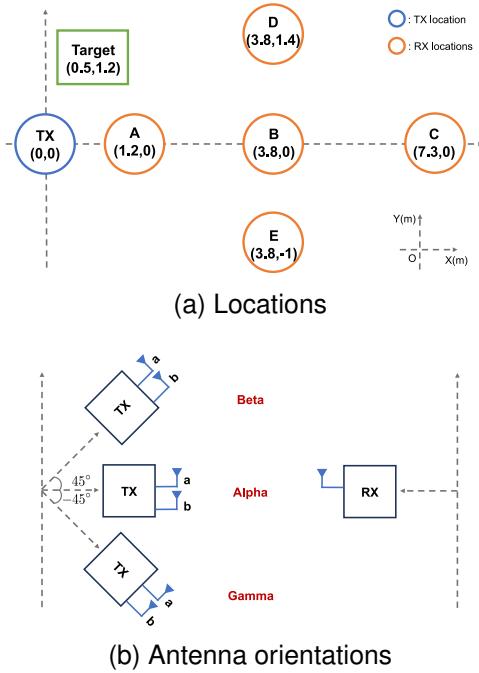


Fig. 2: Locations and antenna orientations setup.

i.e., A to E, by setting the TX location as the origin, and the relative xy positions are represented. In addition, for each RX location, three different antenna orientations, i.e., Alpha, Beta, and Gamma, are assumed on the TX side as in Fig. 2b.

### C. System Parametrization

Regarding the system parameterization, we have used a number of  $N_{\text{on}} = 521$  subcarriers centered at  $f_c$ , where the FFT size is set to  $K = 1024$ . The sampling frequency is  $B = 983.04$  Hz so that the bandwidth occupied by the transmitted signal is approximately 500 MHz. For each channel measurement, a window of 1024 samples is averaged 100 times at the RFSoc ZCU111 to increase the SNR prior to channel estimation. Then, 100 channel estimates are collected at the host computer for offline processing.

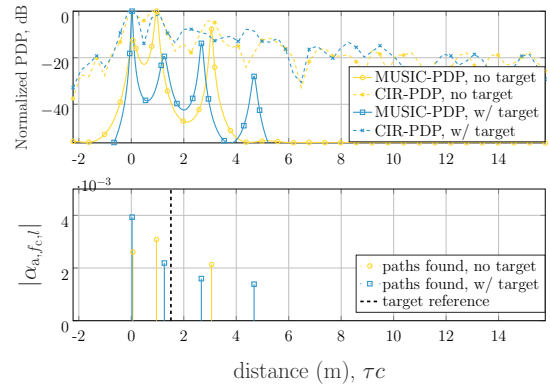


Fig. 3: **Upper part:** The smoothed MUSIC-PDP vs a classical CIR-PDP. **Lower part:** The estimated path gains per path delay. The vertical dashed line corresponds to the target location only when a target of interest is present, and  $\tau_c$  is the additional distance traveled by the path in relation to the line-of-sight.

## V. EXPERIMENTAL RESULTS

### A. Comparison between CIR and MUSIC-PDP

In Fig. 3, we analyze the instantaneous MUSIC-PDP after frequency smoothing, whilst comparing it with the CIR-PDP obtained from (4). Clearly, the frequency-smoothed MUSIC-PDP provides a refined estimation of the multipath channel via its orthogonality features, given a good model order selection, e.g. the elbow method. It is worth noting that the estimator can in some cases capture an estimate multipath with a delay closely matching a path reflected by the target, as can be seen in Fig. 3. Also, when the target is placed, a new path is created at around 4.7 m which is a result of multiple bounces in the indoor environment.

In the following subsection, we provide a statistical analysis of how the number of multipath changes with and without the target for different frequencies.

### B. Multi-band Analysis

In Fig. 4, we present histograms of the estimated number of multipath components at 6.5 GHz, comparing scenarios with and without a target for various orientations. The case of 8.75 GHz is shown in Fig. 5. The histogram was computed by estimating the number of multipath components over all positions and antennas.

For orientation Beta and frequency 6.5 GHz, Fig. 4, we see that the mode of the histogram occurs at 4 when no target is present as compared to 5 when the target is present. A different behavior occurs at 8.75 GHz, Fig. 5, where a mode without a target is 4 as compared to 2 when a target is present. For orientation Alpha in the 6.5 GHz band, the histogram mode is at 3 when no target is present, increasing to 4 with the target reflector. Interestingly, at a higher frequency of 8.75 GHz, the mode shifts to 5 without a target and decreases to 3 when a target is present. Averaging across all orientations (namely Alpha, Beta, and Gamma), Fig. 4 shows the histogram mode

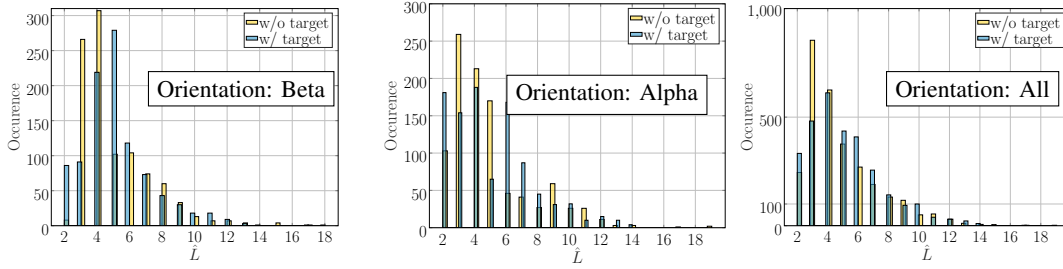


Fig. 4: Frequency 6.5 GHz. Histograms of the estimated number of multipath components, with and without target.

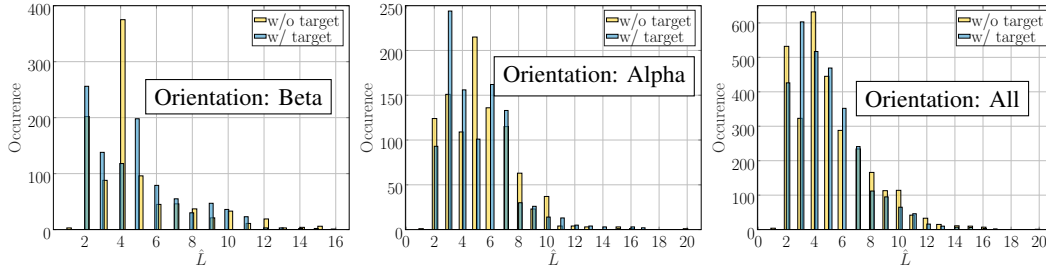


Fig. 5: Frequency 8.75 GHz. Histograms of the estimated number of multipath components, with and without target.

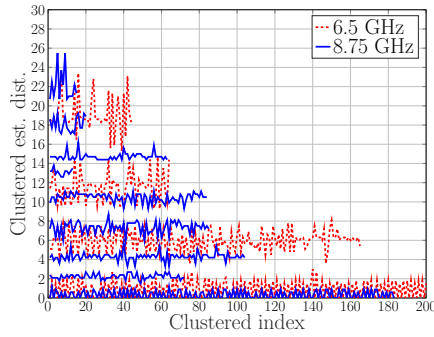


Fig. 6: The  $K$ -means clustered paths for 6.5 GHz and 8.75 GHz showing path distances as a function of their index.

at 3 without a target, which rises to 4 when the target reflector is introduced. Notably, at the higher frequency of 8.75 GHz, illustrated in Fig. 5, the mode changes to 4 in the absence of a target and drops to 3 when a target is present.

These observations highlight the frequency-dependent nature of multipath components in the presence of a target reflector. At lower frequencies, such as 6.5 GHz, longer wavelengths tend to diffract around obstacles, maintaining or even increasing the number of observed multipath components when a target is introduced, as evidenced by shifts in histogram modes across orientations. Higher frequencies, like 8.75 GHz, tend to behave differently. Due to their shorter wavelengths, they are more susceptible to blockage and reflection effects, which can reduce the multipath component density when a target is present. This phenomenon is particularly apparent in orientation Beta, where the histogram mode decreases from 4 to 2 with the target.

In Fig. 6, we plot the  $K$ -means output where each line

shows the delay estimates, translated into distances, as a function of the clustering index. The clustering index is used to index the delay estimates belonging to a single cluster. It appears that  $K$ -means clustering can classify more stable paths at the higher frequency, i.e. at 8.75 GHz, as compared to the lower frequencies. Moreover, there appear to be paths that fluctuate for both frequencies, after clustering, with more fluctuations at lower frequencies. We can also see that  $K$ -means can distinguish more paths at higher frequencies than those at lower ones. This can also indicate that *higher frequencies can promote more distinguishable paths*.

### C. Insights for Multi-Band Sensing

In the following, we provide an illustration of the data to better understand the results of Figs. 4, 5, and 6, which is also an insightful analysis of the impact of the frequency on ISAC. The delay axis is given is converted to traveled by the path. Our approach is to provide a brief illustration of how the energy distribution on the channel impulse changes with the presence of the target in some cases. We define two energy regions on the channel impulse response, namely, *positive* ( $P$ ) and *negative* ( $N$ ).

- $P$ -region: parts of the channel where new reflections are created. These regions are particularly interesting for bistatic sensing because the new paths do not interfere with the clutter in the time domain, facilitating sensing. While typical bistatic sensing models rely on a single bounce from the target to the receiver, the  $P$ -region can contain late paths that also convey information about the target.
- $N$ -region: parts of the channel where paths are blocked. Another approach to perform sensing is to analyze the multipath components that are suppressed in the presence of the target. When prior knowledge of the clutter is

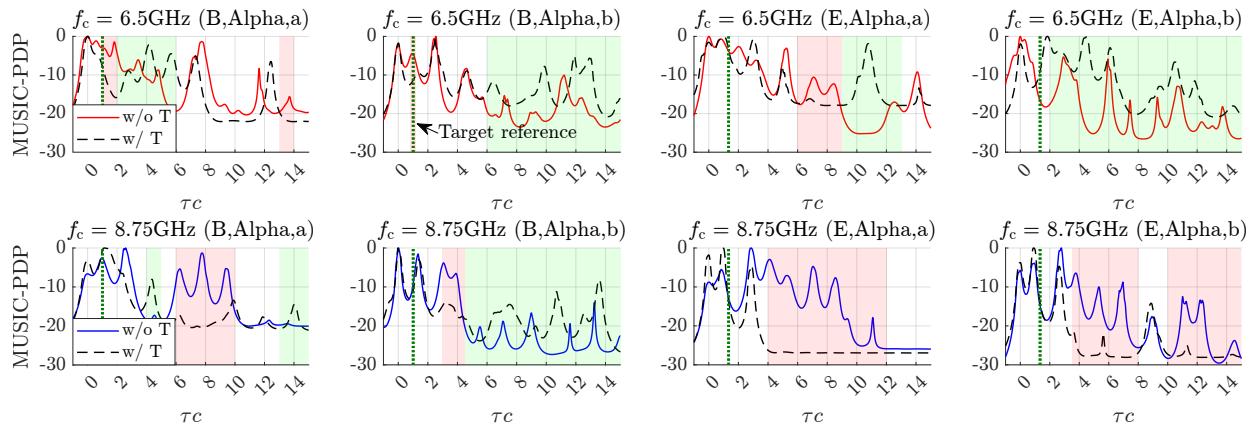


Fig. 7: MUSIC-PDP with  $P$ -region (green shaded) and  $N$ -region (red shaded), with and without target (T).

available, this can be an invaluable source of information to infer the target's spatial characteristics.

The results are shown in Fig. 7. As predicted by the histograms of Fig. 4, we observe that the 6.5 GHz frequency has a tendency to have newer paths with the target ( $P$ -region with green shaded areas), while the 8.75 GHz has more blockage ( $N$ -region with red shaded areas). In general, these results indicate that *one effective way to perform sensing in high frequencies is by analyzing the clutter blockage, while lower frequencies create late paths (multi-bounce) with higher energy.*

## VI. CONCLUSION

In this paper, we conducted a set of indoor channel measurements for the low FR3 frequencies 6.5 GHz and 8.75 GHz, using the Pi-Radio FR3 front-end board which allows generating RF signals anywhere between 6 GHz and 24 GHz. In addition to multi-band, we also measured the channel in the presence of a target to investigate sensing aspects. To analyze the data, we have used an established post-processing methodology based on MUSIC, which provides a refined estimation of the channel impulse response delays. The analysis revealed that in the presence of the target, the 6.5 GHz has a tendency to add new distinguishable reflections, while the higher frequency 8.75 GHz is more susceptible to blockage.

The methodology presented in this paper to measure sensing and communication aspects of the channel in a multi-band setting will serve as a guideline for future work. In particular, we plan to extend this analysis by characterizing spatial-frequency features across the entire FR3 spectrum.

## REFERENCES

- [1] M. Chafii, L. Bariah, S. Muhaidat, and M. Debbah, "Twelve scientific challenges for 6G: Rethinking the foundations of communications theory," *IEEE Commun. Surv. Tutor.*, vol. 25, no. 2, pp. 868–904, 2023.
- [2] S. Kang, M. Mezzavilla, S. Rangan, A. Madanayake, S. B. Venkatakrisnan, G. Hellboug, M. Ghosh, H. Rahmani, and A. Dhananjay, "Cellular wireless networks in the upper mid-band," *IEEE Open J. Commun. Soc.*, Mar. 2024.
- [3] FCC, "Notice of Proposed Rulemaking: Expanding Flexible Use of the 12.2-12.7 GHz Band," *Docket No. 20-443*, vol. FCC-21-13, 2021.
- [4] T. S. Rappaport, D. Shakya, and M. Ying, "Point data for site-specific mid-band radio propagation channel statistics in the indoor hotspot (InH) environment for 3GPP and next generation alliance (NGA) channel modeling," *arXiv preprint arXiv:2409.19873*, 2024.
- [5] D. Shakya *et al.*, "Urban Outdoor Propagation Measurements and Channel Models at 6.75 GHz FR1(C) and 16.95 GHz FR3 Upper Mid-band Spectrum for 5G and 6G," in *IEEE International Conference on Communications (ICC)*, Montreal, Canada, June 2025, pp. 1–6, (submitted).
- [6] M. Mezzavilla, A. Dhananjay, M. Zappe, and S. Rangan, "A frequency hopping software-defined radio platform for communications and sensing in the upper mid-band," in *Proc. IEEE 25th International Workshop on Signal Processing Advances in Wireless Communications (SPAWC)*, Lucca, Italy, 2024, pp. 611–615.
- [7] Y. Hu, M. Yin, M. Mezzavilla, H. Guo, and S. Rangan, "Channel modeling for FR3 upper mid-band via Generative Adversarial Networks," in *Proc. IEEE SPAWC*, Lucca, Italy, 2024, pp. 776–780.
- [8] F. Liu *et al.*, "Integrated sensing and communications: Toward dual-functional wireless networks for 6G and beyond," *IEEE J. Sel. Areas Commun.*, vol. 40, no. 6, pp. 1728–1767, 2022.
- [9] R. Bomfin and M. Chafii, "Unique word-based frame design for bistatic integrated sensing and communication," pp. 1–1, 2024.
- [10] A. Bazzi and M. Chafii, "On outage-based beamforming design for dual-functional radar-communication 6G systems," *IEEE Transactions on Wireless Communications*, vol. 22, no. 8, pp. 5598–5612, 2023.
- [11] —, "Secure Full Duplex Integrated Sensing and Communications," *IEEE Transactions on Information Forensics and Security*, vol. 19, pp. 2082–2097, 2024.
- [12] R. Bomfin, Z. Li, A. Nimr, and G. Fettweis, "Experimental validation of superresolution delay estimation algorithm using a 26 GHz radar setup," in *2022 2nd IEEE International Symposium on Joint Communications & Sensing (JC&S)*, 2022, pp. 1–6.
- [13] R. Bomfin, M. Chafii, A. Nimr, and G. Fettweis, "Channel estimation for MIMO space time coded OTFS under doubly selective channels," in *2021 IEEE International Conference on Communications Workshops (ICC Workshops)*, 2021, pp. 1–6.
- [14] A. Bazzi, D. T. M. Slock, and L. Meilhac, "On mutual coupling for ULAs: Estimating AoAs in the presence of more coupling parameters," in *2017 IEEE International Conference on Acoustics, Speech and Signal Processing (ICASSP)*, 2017, pp. 3361–3365.
- [15] P. Closas and C. Fernandez-Prades, "A statistical multipath detector for antenna array based GNSS receivers," *IEEE Transactions on Wireless Communications*, vol. 10, no. 3, pp. 916–929, 2011.
- [16] A. Bazzi, D. T. M. Slock, and L. Meilhac, "On spatio-frequential smoothing for joint angles and times of arrival estimation of multipaths," in *2016 IEEE International Conference on Acoustics, Speech and Signal Processing (ICASSP)*, 2016, pp. 3311–3315.
- [17] I. T. Jolliffe, *Principal component analysis for special types of data*. Springer, 2002.